Dynamic Multiaxial Behaviors of 3D Shape Memory Alloy Nanowires: A Phase-Field Study

R. Dhote[1], K. Behdinan[1], H. Gomez[2]

[1]Mechanical and Industrial Engineering, University of Toronto,
5 King's College Road, Toronto, ON, M5S 3G8, Canada.
[2]Department of Applied Mathematics, University of A Coruña
Campus de Elvina, s/n. 15192 A Coruña, Spain.

Abstract

In this paper, we focus on the dynamic multiaxial behaviors of shape memory alloy (SMA) rectangular prismatic nanowires. A strain-based order parameter 3D phase-field model is used to study the microstructure evolution and its consequent thermo-mechanical behaviors in the cubic-to-tetragonal martensitic phase transformations in SMA nanowires. The FePd nanowire is subjected to displacement based axial-transverse and axial-torsion loadings paths. The numerical results demonstrate the strong influence of multiaxial loadings on microstructures and thermo-mechanical response. The variation of thermo-mechanical response stems from the nucleation of energetically favorable martensitic variants to the applied loading paths. The understanding of multiaxial thermo-mechanical response of nanowires is essential in developing better SMA based devices.

Keywords: Phase-field model, Ginzburg-Landau theory, nonlinear thermo-elasticity, shape memory alloys, nanostructures.

1   Introduction

Shape memory alloys (SMAs) exhibit structural phase transformations in a form of martensitic transformations (MTs) that involve diffusionless affine deformation of atomic unit cell in a sense of the point group theory. A crystallographic high symmetry austenite (A) phase can be transformed into equivalent crystallographic lower symmetry martensite variants (M_i). These phase transformations yield two unique properties of SMAs namely; shape memory effect and pseudoelasticity [1]. These properties have been extensively studied under uniaxial response of SMA wires and exploited successfully in commercial applications [2, 3].

In contrast to conventional applications of SMA wires in uniaxial loadings, modern engineering SMA based 3D devices interact with their environment and are often subjected to complex multiaxial loadings. The development of sophisticated SMA based devices, in bioengineering, micro- and nano-technology fields [4, 5, 6, 7], reveals the necessity to investigate their material properties subjected to complex loadings. The influence of multi-axial loading paths on microstructure evolution and its consequent effects on thermo-mechanical behavior is essential for development of better SMA-based devices.

Extensive experiments on SMA wires revealed their uniaxial loading behavior for stress induced loadings in research and commercial applications. A comprehensive review of uniaxial SMA behaviors can be found in [1, 2, 3, 8, 9]. There is limited experimental research on the multiaxial behavior of SMAs. The strong influence of tension-torsion loadings on macroscopic SMA material behavior were experimentally studied by Tokuda et al. [10], Sittner et al. [11], Lim and McDowell [12], Bouvet et al. [13], McNaney et al. [14], Lavernhe-Taillard et al. [15] and Grabe and Bruhns [16] among others. These experimental studies revealed that variations in SMA material response emerge from nucleation of energetically favorable martensitic variants to the applied loadings. The majority of

these multiaxial experimental studies focused on the macroscopic behavior of SMAs with a little focus on underlying MTs and how MTs affect the thermo-mechanical response.

There is a plethora of modeling literature to describe uniaxial behavior of SMAs [2, 8, 9, 17, 18, 19]. In order to model the SMA material response for advanced engineering applications, different multiaxial models have been proposed. The models based on the crystal plasticity, micromechanics and phenomenological approaches [20, 21, 22, 23, 24, 25] have been developed to predict complex loading path dependence due to reorientation of the constituent phases in SMAs. In this paper, we focus on a phenomenological approach based on the phase-field (PF) theory, which has emerged as a powerful computational material modeling approach for phase transforming materials [26]. PF models have been increasingly used for solid-to-solid phase transformations in SMAs at different length scales [27, 28, 29, 26, 30, 31, 32, 33, 34, 35]. The majority of the studies based on PF models have focused on the microstucture evolution and uniaxial properties of SMA nanostructures [31, 33, 36, 37]. However, as mentioned earlier, modern engineering applications may induce multi-axial loadings on SMA structures during interactions with its environment. The investigation of multiaxial behaviors of 2D SMA nanowires using the PF model was analyzed by Dhote et al. [38]. The study revealed that detwinning is a prominent phase transformation mechanism during axial loading, while the redistribution of martensitic variants based on the local axial stress sign is prominent during the bending load. Though the study provided an insight into the phase transformations and their consequent effect on the thermo-mechanical behavior, the 2D model suffers severe limitation, with the effect of martesitic variant in the third dimension totally neglected. As the phase transformations occur under preferential directions in 3D planes, there is an accommodation of strain in three spatial directions. Hence, it is essential to incorporate the effect of martensitic variants in all the three directions and study the properties of SMAs using the full 3D model.

This paper focuses on the microstructure evolution and thermo-mechanical behavior of 3D SMA nanowires subjected to multiaxial loading paths. We use the 3D PF model and numerical framework developed in Dhote et al. [39] to simulate the cubic-to-tetragonal phase transformations in SMAs. This model has been used to study the stress-induced phase transformations in nanowires under uni-axial ramp loading-unloading paths [40]. The main objective of this paper is to study the multiaxial behavior of SMA nanowires under a combination of axial, transverse, and torsion loading-unloading paths. To the best of our knowledge, here we present the first dynamic multiaxial behaviors of SMA nanowires using the 3D PF model.

The paper is organized as follows: first, we briefly describe the governing equations of 3D dynamic coupled thermo-mechanical PF model and its numerical formulation using isogeometric analysis in section 2. In section 3, we conduct numerical simulations on SMA nanowires under multiaxial loading paths and study the microstructure morphology evolution and how it affects the shape memory effect and pseudoelastic behaviors. Finally, the conclusions are summarized in section 4.

2   3D Model and Numerical Formulation

The governing equations of the dynamic thermo-mechanical model for SMAs have been derived using the Ginzburg-Landau energy and the phase-field (PF) theory. Here, we focus on the cubic-to-tetragonal PT, where the cube represents the A phase, and the three tetragonal phases represent $M_{i,i=1,2,3}$. The complete derivation of the model is described in Dhote et al. [39]. For consistency and completeness, the highlights of the model and numerical implementation are summarized as follows.

2.1 Dynamic Thermo-Mechanical Phase-Field Model

The cubic-to-tetragonal phase transformation can be described using the free-energy functional $\mathscr{F}$ [41, 31] as

$$
\mathscr{F}[\boldsymbol{u}, \theta] = \int_{\Omega} \left[\frac{a_1}{2} e_1^2 + \frac{a_2}{2} \left(e_4^2 + e_5^2 + e_6^2 \right) + a_3 \tau \left(e_2^2 + e_3^2 \right) + a_4 e_3 \left(e_3^2 - 3 e_2^2 \right) \right.
$$
$$
\left. + a_5 (e_2^2 + e_3^2)^2 + \frac{k_g}{2} \left(|\nabla e_2|^2 + |\nabla e_3|^2 \right) \right] \mathrm{d}\Omega, \tag{1}
$$

where a_i are constants that define the mechanical properties of the material, k_g is the gradient energy coefficient, τ is the dimensionless temperature defined as $\tau = (\theta - \theta_m)/(\theta_0 - \theta_m)$, where θ_0 and θ_m are the phase transformation temperatures, and $|\cdot|$ denotes the Euclidean norm of a vector.

In Eq. (1), e_1 represents the hydrostatic strain, e_2 and e_3 represent the deviatoric strains, and e_4, e_5, e_6 represent the shear strains. The deviatoric strains e_2 and e_3 are selected as an order parameters (OPs) to distinguish different phases in the domain. The strain measures $\boldsymbol{e} = \{e_1 \; e_2 \; e_3 \; e_4 \; e_5 \; e_6\}^T$ are defined in terms of the Cauchy-Lagrange infinitesimal strain tensor $\boldsymbol{\epsilon} = \{\epsilon_{11} \; \epsilon_{22} \; \epsilon_{33} \; \epsilon_{23} \; \epsilon_{13} \; \epsilon_{12}\}^T$ in Eq. (2).

$$
\boldsymbol{e} = \left[\begin{array}{c|c} \mathbb{D}_3 & \mathbb{O}_3 \\ \hline \mathbb{O}_3 & \mathbb{I}_3 \end{array} \right] \boldsymbol{\epsilon}, \qquad \mathbb{D}_3 = \begin{bmatrix} 1/\sqrt{3} & 1/\sqrt{3} & 1/\sqrt{3} \\ 1/\sqrt{2} & -1/\sqrt{2} & 0 \\ 1/\sqrt{6} & -1/\sqrt{6} & -2/\sqrt{6} \end{bmatrix}, \tag{2}
$$

where the $\mathbb{I}_3$, and $\mathbb{O}_3$ are the 3×3 identity and zeros matrices, respectively. The strain components are defined as $\epsilon_{ij} = (u_{i,j} + u_{j,i})/2$, $i, j \in \{1, 2, 3\}$, where subscripts after comma denote partial differentiation. The unknowns are the displacement field $\boldsymbol{u} = \{u_1, u_2, u_3\}^T$ and the temperature θ in the physical domain $\Omega \subset \mathbb{R}^3$, which is an open set parameterized by Cartesian coordinates $\boldsymbol{x} = \{x_1, x_2, x_3\}^T$. The Raleigh dissipation is incorporated to dampen the motion of domain walls during the phase transformation [31, 42]. The dissipation functional $\mathscr{R}$, the dissipation stress tensor $\boldsymbol{\sigma}' = \{\sigma_{ij}'\}$ and stress tensor $\boldsymbol{\sigma} = \{\sigma_{ij}\}$ are defined as

$$
\mathscr{R} = \int_{\Omega} \frac{\eta}{2} |\dot{\boldsymbol{e}}|^2 \, \mathrm{d}\Omega, \qquad \sigma_{ij}' = \left[\begin{array}{c|c} \mathbb{D}_3^T & \mathbb{O}_3 \\ \hline \mathbb{O}_3 & \frac{1}{2}\mathbb{I}_3 \end{array} \right] \dot{e}_i, \qquad \sigma_{ij} = \frac{\partial \mathscr{F}}{\partial \epsilon_{ij}}, \tag{3}
$$

where $\dot{\boldsymbol{e}} = \{\dot{e}_i\}_{i=1,\ldots,6}$ is the time derivative of strain.

Using Hamiltonian mechanics and conservation of energy, the system of governing equations can be derived. Adding suitable boundary and initial conditions, we get the problem as follows:

$$
\begin{array}{lll}
\rho \ddot{u}_i = \sigma_{ij,j} + \eta \sigma_{ij,j}' + \mu_{ij,kkj} + f_i, & \text{in } \Omega \times (0, T), & (4.1) \\[4pt]
c_v \dot{\theta} = \kappa \theta_{,ii} + \Xi \theta \left(u_{i,i} \dot{u}_{j,j} - 3 u_{i,i} \dot{u}_{i,i} \right) + g, & \text{in } \Omega \times (0, T), & (4.2) \\[4pt]
\mu_{ij,k} n_k = 0, & \text{on } \Gamma \times (0, T), & (4.3) \\[4pt]
\left(\sigma_{ij} + \eta \sigma_{ij}' + \Delta \mu_{ij} \right) n_j = 0, & \text{on } \Gamma_{Si} \times (0, T), & (4.4) \\[4pt]
u_i = u_i^D, & \text{on } \Gamma_{Di} \times (0, T), & (4.5) \\[4pt]
\theta_{,i} n_i = 0, & \text{on } \Gamma \times (0, T), & (4.6) \\[4pt]
u_i(\boldsymbol{x}, 0) = u_i^0(\boldsymbol{x}), & \text{in } \overline{\Omega}, & (4.7) \\[4pt]
\theta(\boldsymbol{x}, 0) = \theta^0(\boldsymbol{x}), & \text{in } \overline{\Omega}, & (4.8)
\end{array}
$$

where f_i is the external mechanical load, g is the external thermal load, ρ is the density, η is the viscous dissipation, c_v is the specific heat, κ is the thermal conductance coefficient, and Ξ is the

strength of the thermo-mechanical coupling. Γ is the boundary of Ω with $\Gamma = \overline{\Gamma_{Di} \cup \Gamma_{Si}}$, $\boldsymbol{n}$ is the outward normal, u_i^0 and θ_0 are given functions, which represent the initial displacements, and temperature in the closed domain $\overline{\Omega}$.

The model described in Eqs. (4.1)–(4.2) consists of the bidirectional coupling between structural and thermal fields via θ, u_i and $\dot{u}_{i,j}$. The constitutive equations σ_{ij} that describe the cubic-to-tetragonal PT are highly non-linear to account for the shape memory effect and pseudoelastic hysteretic properties (see [39]). The thermo-mechanical coupling, non-linear hysteresis properties and fourth-order spatial differential terms in the 3D model impose several numerical challenges. An isogeometric analysis (IGA) has been successfully used to obtain the numerical solutions to a number of important problems [43]. We have used an IGA framework for the numerical solution of the developed 3D PF model.

2.2 Numerical Formulation

To implement the 3D PF model in an IGA framework, the weak formulation of Eqs. (4.1)–(4.2) is derived by multiplying the equations with weighing functions $\{\boldsymbol{w}, q\}$, integrating them over Ω and transforming them by using the integration by parts. Let X denote both the trial solution and weighting function spaces, which are assumed to be identical. Let $(\cdot, \cdot)_\Omega$ denote the $\mathcal{L}^2$ inner product with respect to the domain Ω. The variational formulation is stated as follows:
Find solution $\boldsymbol{S} = \{\boldsymbol{u}, \theta\} \in X$ such that $\forall \boldsymbol{W} = \{\boldsymbol{w}, q\} \in X : B(\boldsymbol{S}, \boldsymbol{W}) = 0$, with

$$
\begin{aligned}
\mathsf{B}(\mathsf{S},\mathsf{W}) = \quad & \big(w_i, (\rho\ddot{u}_i - f_i)\big) + \big(w_{i,j}, \sigma_{ij} + \eta\sigma'_{ij}\big) - \big(w_{i,jk}, \mu_{ij,k}\big) \\
+ \quad & \Big(q, \Big(c_v\dot{\theta} - \Xi\theta(u_{i,i}\dot{u}_{j,j} - 3u_{i,i}\dot{u}_{i,i}) - g\Big)\Big) + (\kappa q_{,i}, \theta_{,i}).
\end{aligned}
\tag{5}
$$

The semi-discrete formulation is used for solving Eq. (5). We use the Galerkin method to discretize the space and treat the time as continuous. The variational problem over the finite-dimensional spaces may be stated as follows: $\mathsf{B}(\mathsf{S}^{\boldsymbol{h}}, \mathsf{W}^{\boldsymbol{h}}) = 0$, where

$$
\mathsf{W}^h = \{\boldsymbol{w}^h, q^h\}, \quad w_i^h(\boldsymbol{x}, t) = \sum_{A=1}^{n_b} w_{iA}(t)N_A(\boldsymbol{x}), \quad q^h(\boldsymbol{x}, t) = \sum_{A=1}^{n_b} q_A(t)N_A(\boldsymbol{x}),
\tag{6}
$$

where the N_A's are the basis functions, and n_b is the dimension of the discrete space. In the context of the IGA, the N_A are non-rational B-spline (NURBS) functions. IGA offers unique advantages in solving problems involving higher-order PDEs such as higher-order accuracy, robustness, geometric flexibility, compact support, and $\mathscr{C}^1-$ or higher-order inter-element continuity. Time discritization is performed by the generalized–α method. The readers are referred to Dhote et al. [39] for details about the geometric flexibility, higher-order continuity and mesh convergence studies for the model in section 2.1. In this manuscript, we have modified the IGA framework to incorporate multiaxial loading paths to study the dynamic thermo-mechanical behaviors of SMA nanowires.

3 Numerical Simulations

Here, we conduct multiaxial loading-unloading simulations on rectangular prismatic nanowires under dynamic loading conditions. The nanowires of dimension $150\times37.5\times37.5$ nm are meshed with $80\times20\times20$ $\mathscr{C}^1$-continuous B-spline basis functions. We remark that the system of governing Eqs. (4.1)–(4.2) is first rescaled and implemented in the IGA framework, and the results are calculated back in the dimensional form. The $Fe_{70}Pd_{30}$ material properties [31, 44] used for the SMA nanowires are summarized as: $a_1 = 192.3$ GPa, $a_2 = 280$ GPa, $a_3 = 19.7$ GPa, $a_4 = 2.59\times 10^3$ GPa, $a_5 = 8.52\times$

10^4 GPa, $k_g = 3.15 \times 10^{-8}$ N, $\theta_{\mathrm{m}} = 270$ K, $\theta_0 = 295$ K, $c_v = 350$ Jkg^{-1}K^{-1}, $\kappa = 78$ Wm^{-1}K^{-1}, and $\rho = 10000$ kg m^{-3}.

The nanowire is constrained at one end, and the other end is displaced by χ_i in x_i directions and/or rotated by χ_θ about x_1 in the counterclockwise direction (see inset diagrams in Fig. 1). We assume the nanowire in a thermally insulated environment. The multiaxial responses of the SMA nanowire are investigated for the shape memory effect and pseduoelastic behavior as described below.

3.1 Shape Memory Effect (SME)

SMAs manifest the SME behavior below the transition temperature. To define the initial state of the nanowire, we use small random displacement $\boldsymbol{u}$ with normally constrained surfaces and quench it to temperature corresponding to $\tau = -1.2$. The specimen was allowed to evolve until the microstructure and energy get stabilized. The self-accommodated twinned martensitic variants M_1, M_2, and M_3 shown in red, blue, and green colors, respectively, are evolved in approximately equal proportions as shown in Fig. 2(a). The evolved twinned microstructure in nanowire is taken as an initial condition and subjected to the following three loading paths:

- type I - axial loading ($\chi_1 \neq 0$, $\chi_2 = \chi_3 = \chi_\theta = 0$)
- type II - combination of axial and transverse loadings ($\chi_1 \neq 0$, $\chi_2 \neq 0$, $\chi_3 \neq 0$, $\chi_\theta = 0$)
- type III - combination of axial and torsion loadings ($\chi_1 \neq 0$, $\chi_2 = \chi_3 = 0$, $\chi_\theta \neq 0$).

In all the SME simulations, we load the SMA nanowire to $\chi_1 = 3\%$. The loading of SMA nanowire for type I, type II, and type III paths is presented in Fig. 1.

In the type I loading path, the M_1 martensitic variant is favorable to the axial loading. Under the influence of axial loading, the M_2 and M_3 variants are energetically unfavorable and get converted into the M_1 variant via the detwinning phase transformations ($M_2 \rightarrow M_1$ and $M_3 \rightarrow M_1$) as observed in microstructure morphology evolution in Fig. 2. The average axial stress–strain σ_{11}-ϵ_{11} and dimensionless temperature τ over the volume of nanowire are presented in the solid blue color line in Fig. 5. The SME mechanical hysteresis loop consists of the elastic loading of martensitic variants, and phase transformations is presented in Fig. 5(a). The remnant strain exists at the end of the unloading cycle. The τ evolution, as shown in Fig. 5(b), is qualitatively observed in the experiments [45, 46].

In the type II loading path, the specimen is loaded in the x_2 and x_3 transverse directions with $\chi_2 = \chi_3 = 2\%$ strains in the corresponding direction. The transverse displacements are applied once the axial strain in the nanowire reaches 0.5% to study the effect of multiaxial loadings on the phase transformation plateau. The microstructure morphology evolution in nanowire is presented in Fig. 3. The detwinning phase transformations are predominant prior to the application of the χ_2 and χ_3 loads. On the application of these loadings, the M_2 and M_3 variants become favorable, in addition to the M_1 variant, to the applied loading paths. The microstructure morphology evolution presented in Fig. 3 indicates the generation of the pockets of the M_2 and M_3 variants in the nanowire. The loading of the nanowire in the x_2 and x_3 directions yield in the axial stiffening of the nanowire at higher strains as shown with dashed-dot red color line in Fig. 5(a). Further loading causes formation of the neck region (as shown in the inset) due to the presence of the M_2 and M_3 variants. The complete conversion of $M_2 \rightarrow M_1$ and $M_3 \rightarrow M_1$ takes place at higher stress as seen in the inset in Fig. 5(a) . At the end of unloading, it is observed that the axial remnant strain in type II loading is smaller than the type I loading due to the evolution of M_2 and M_3 variants due to the redistribution of martensites as observed experimentally [47]. The microstructure morphology evolution in the 3D model is qualitatively similar to the 2D PF model in Dhote et al. [38], however, the evolution of all three martensitic variants in the model gives a better understanding of the strain accommodation

in the 3D domain. The effect of transverse load can be observed in Fig. 5(b) as a deviation in τ evolution from type I loading on the application of the transverse loads.

In the type III loading path, the nanowire is subjected to torsion load $\chi_\theta = 5/6\pi$ radian, once the axial strain in the nanowire reaches 0.5%. The microstructure morphology evolution presented in Fig. 4. The shear strains due to the torsion loading do not contribute to the definition of OPs e_2 and e_3, however, their effect can be observed as evolution of different microstructure morphology in Fig. 4 (as compared to Fig. 2). The loading path causes the axial stiffening response as seen in Fig. 5(a) presented as the black dotted line. The shear stresses introduced due to the torsion loading cause the evolution of different microstructure and lead to higher axial stress. The average τ over time is presented in Fig. 5(b).
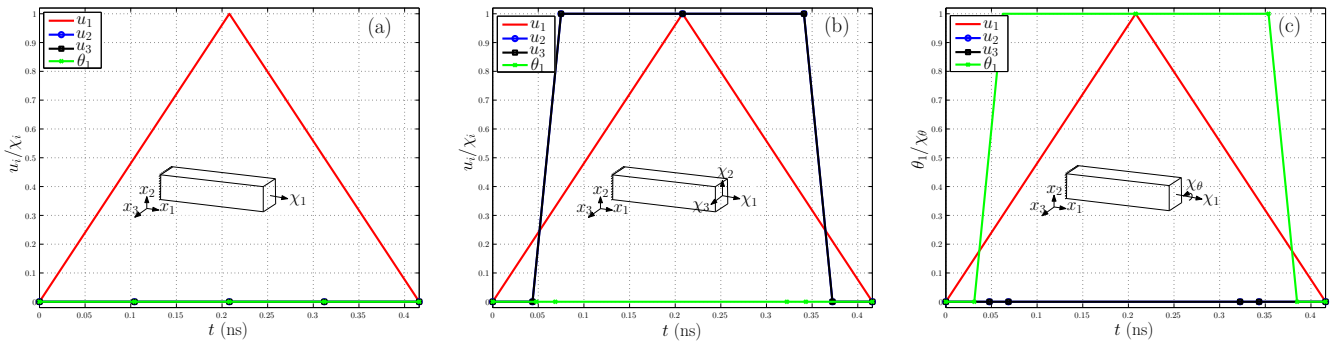
Figure 1: SME loading: (a) type I, (b) type II, and (c) type III paths.
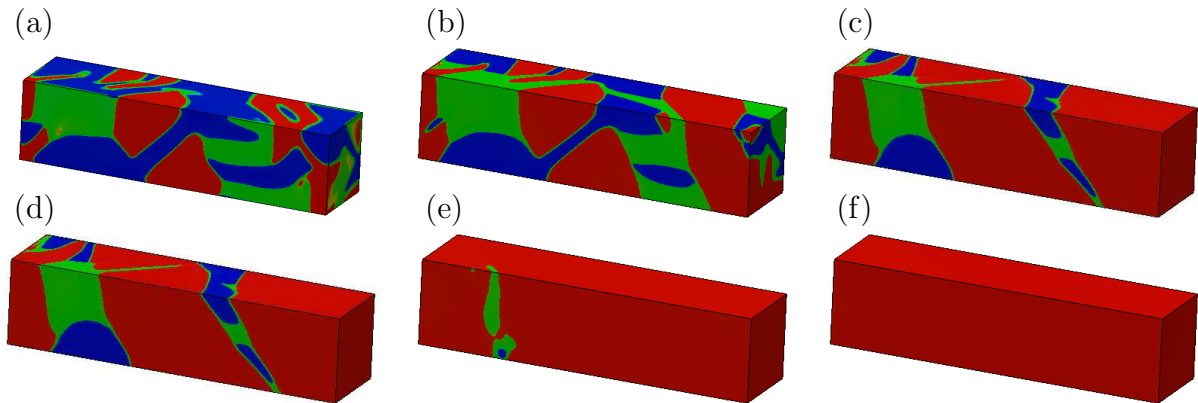
Figure 2: (Color online) SME: microstructure morphology evolution in the nanowire under type I path at time instants t (ns) (a) 0, (b) 0.0415, (c) 0.0833, (d) 0.1, (e) 0.146, (f) 0.208 (red, blue, and green colors represent M_1, M_2, and M_3 variants, respectively).

3.2 Pseudoelastic Behavior (PE)

SMAs manifest the PE behavior above the transition temperature. We follow the two-step procedure described in Sec. 3.1. The nanowire is allowed to evolve to an austenite phase with temperature corresponding to $\tau = 1.12$, starting with a random initial condition of displacement $\boldsymbol{u}$. The austenite phase is taken as an initial condition to the three loading conditions described in Sec. 3.1. In all the PE simulations, the SMA nanowires are loaded to $\chi_1 = 1.25\%$. The loading paths for type I, type II, and type III paths are depicted in Fig. 6. In the microstructure morphology evolution Figs. 7–9, the A, M_1, M_2, and M_3 are shown in yellow, red, blue, and green colors, respectively. The microstructures are purposefully presented in transparent colors to investigate the evolution of different variants inside a domain during the loading-unloading path.
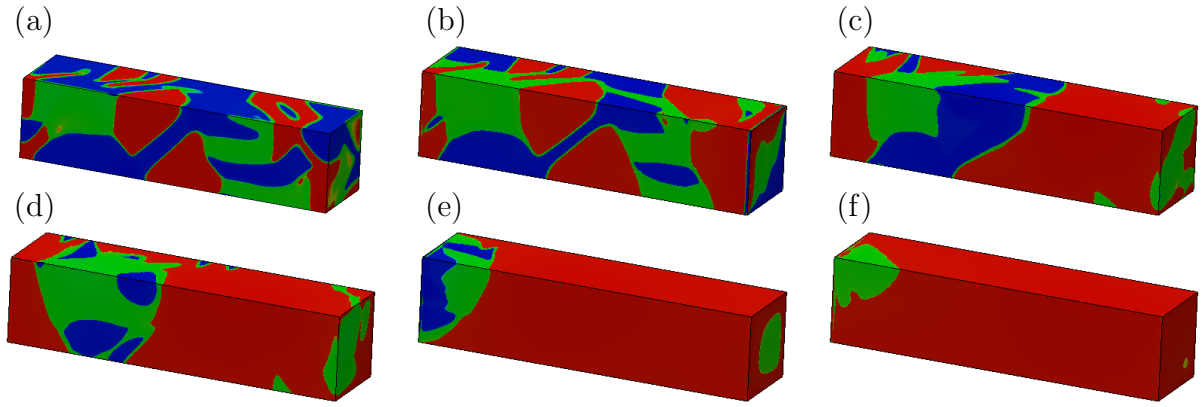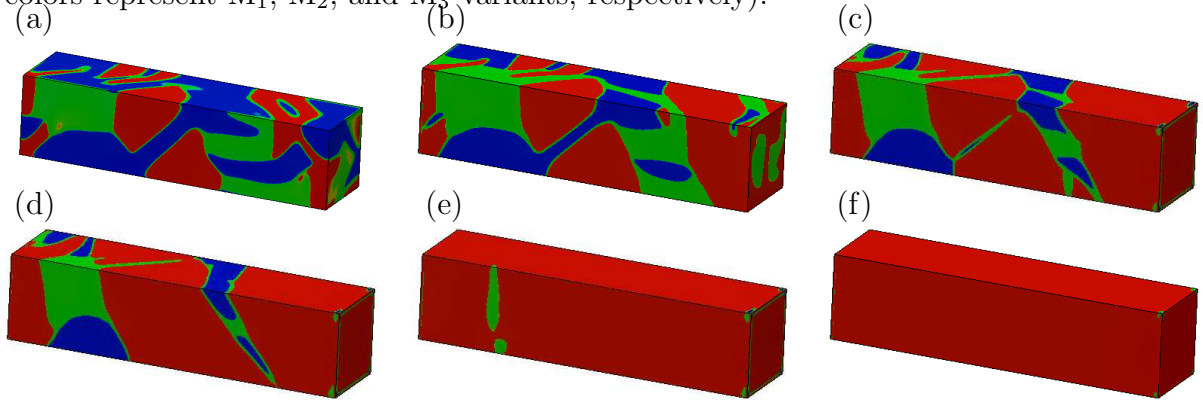
Figure 3: (Color online) SME: microstructure morphology evolution in the nanowire under type II path at time instants t (ns) (a) 0, (b) 0.0415, (c) 0.0833, (d) 0.1, (e) 0.146, (f) 0.208 (red, blue, and green colors represent M_1, M_2, and M_3 variants, respectively).
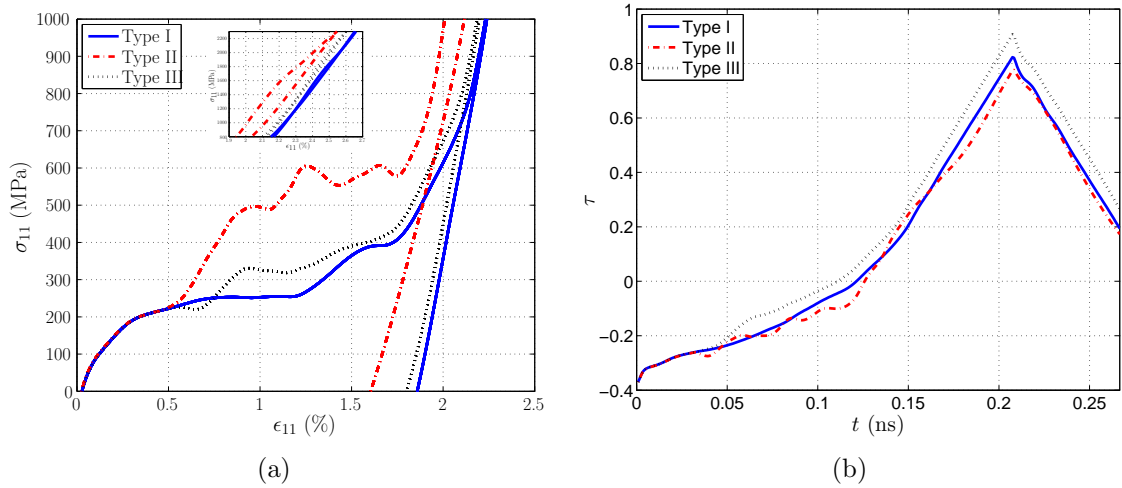

Figure 4: (Color online) SME: microstructure morphology evolution in the nanowire under type III path at time instants t (ns) (a) 0, (b) 0.0415, (c) 0.0833, (d) 0.1, (e) 0.146, (f) 0.208 (red, blue, and green colors represent M_1, M_2, and M_3 variants, respectively).

Figure 5: (Color online) SME: average σ_{11}–ϵ_{11} (a), and time evolution of τ (b) for the type I, II and III multiaxial loading paths.

The time snapshots of microstructure evolution for the type I loading path are presented in Fig. 7. The M_1 variant favors the axial loading and leads to the forward phase transformations A→M_1 during loading stage. The reverse phase transformations M_1→A is active during the unloading stage. At the end of unloading, the nanowire returns to the A phase. The average σ_{11}-ϵ_{11} and τ are presented in Fig. 10 (refer to the solid blue color line). The axial stress-strain curve reproduces hysteretic loop
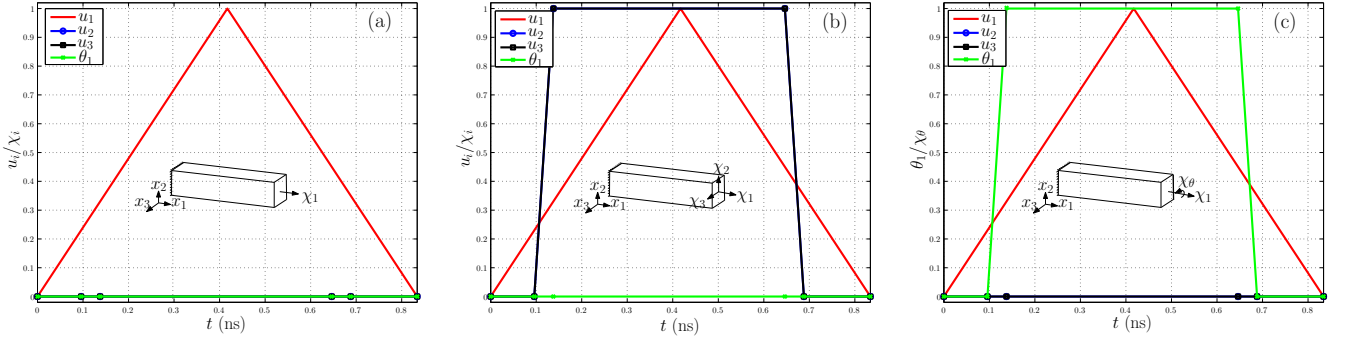
Figure 6: PE loading: (a) type I, (b) type II, and (c) type III paths.

(shown in solid blue color) with a complete recovery of strain at the end of unloading as observed experimentally [45, 2].

In the type II loading path, the nanowire is subjected to displacements in the x_2 and x_3 directions with $\chi_2 = \chi_3 = 1.25\%$ strains in the corresponding directions. The χ_2 and χ_3 displacements are applied when the axial strain in the nanowire reaches 0.3% to study the effect of multiaxial loading on the phase transformation plateau. The time snapshots of microstructure morphology evolution are presented in Fig. 8. The A→M_1 is the primary phase transformation before the application of the transverse direction displacement loads. On the χ_2 and χ_3 displacements, the M_2 and M_3 variants become favorable to the applied loading paths. The pockets of M_2 and M_3 variants are revealed on the longitudinal edges of the nanowire. These pockets of variants travel from the loading surface to the constrained surface on the diagonally opposite edges. The evolution of the M_2 and M_3 variants cause relaxation in the axial stress as observed from the Fig. 10(a) (refer to the red dash-dot line). On further loading, the M_2 and M_3 variants diminish, and the M_1 variant becomes the primary variant. This causes the nanowire to attain a particular stress at a lower strain value. The evolution of average τ over time is presented in Fig. 10(b).

In the type III loading path, the torsion $\chi_\theta = \pi/3$ radians is applied to the nanowire, once the axial strain reaches the 0.3%. On the application of the torsion load, the shear stresses are introduced on the torsion loading. As the shear stress (or strain) does not contribute to the evolution of M_2 and M_3 variants, the M_1 variant is still a predominant variant. However, the effect of the torsion is observed on the average σ_{11}-ϵ_{11} curve, with an axial relaxation of the nanowire. The shear bands can be seen on the loading surface edges. On further loading, the nanowire attains a particular stress at a lower strain value. The evolution of average τ over time is presented in Fig. 10(b)

4 Conclusions

The numerical experiments on the SMA nanowire have demonstrated the influence of multiaxial loading paths on microstructure and thermo-mechanical response. The pure axial loading is dominated by the detwinning phase transformations (M_2→M_1 and M_3→M_1) in SME or A→M_1 in PE. The multiaxial loading energetically activates the other variants and the energetic interaction of M_i-M_j variant leads to a significant variation of the thermo-mechanical behavior. Particularly, we observed that a nanowire shows axial stiffening in shape memory effect and axial relaxation during the pseudoelastic behavior. The multiaxial behavior gives important insights to the response of SMA nanostructures, which can be used in the development of better SMA-based devices.
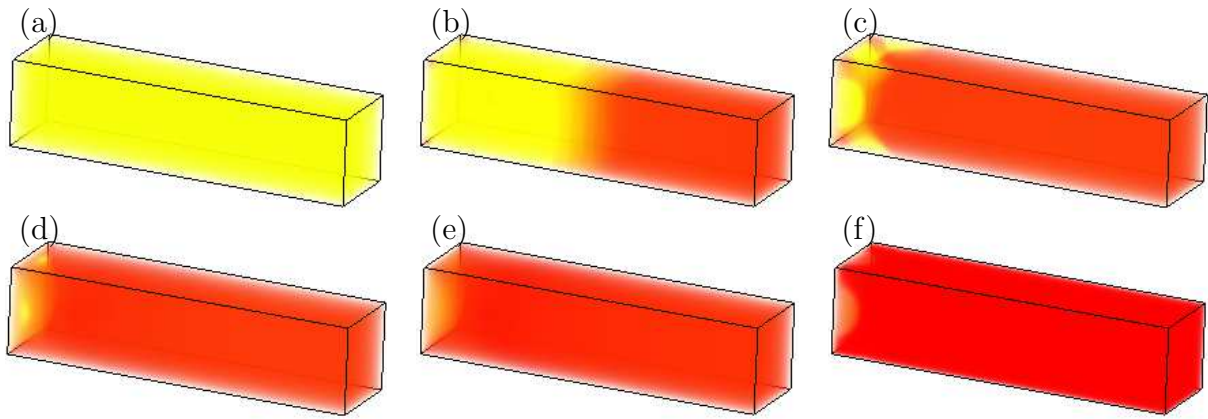
Figure 7: (Color online) PE: microstructure morphology evolution in the nanowire under type I loading path at time instants t (ns) (a) 0,(b) 0.067, (c) 0.083, (d) 0.1, (e) 0.1167, (f) 0.416 (red and yellow colors represent M_1 and A variants, respectively). Transparent colors are used to investigate evolution of different variants.
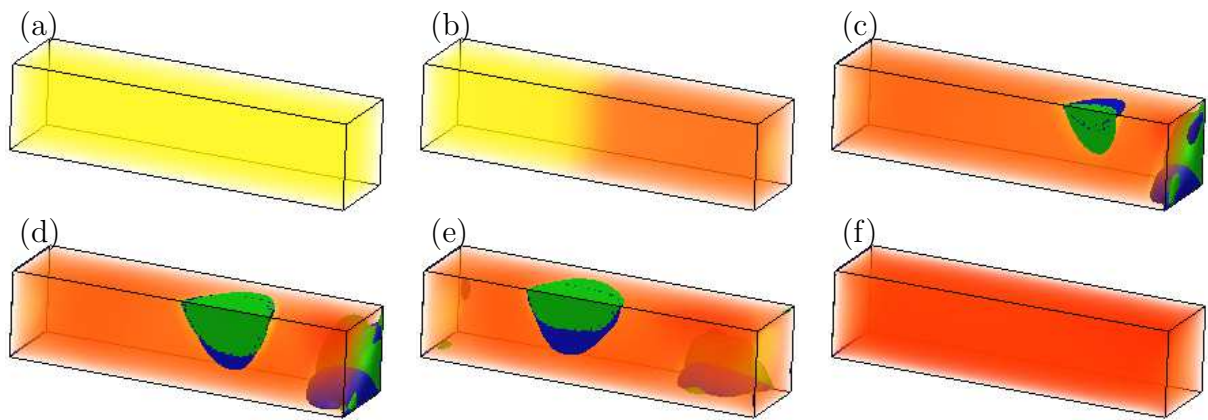

Figure 8: (Color online) PE: microstructure morphology evolution in the nanowire under type II loading path at time instants t (ns) (a) 0, (b) 0.033, (c) 0.1167, (d) 0.133, (e) 0.167, (f) 0.416 (red, blue, green, and yellow colors represent M_1, M_2, M_3, and A variants, respectively). Transparent colors are used to investigate evolution of different variants.
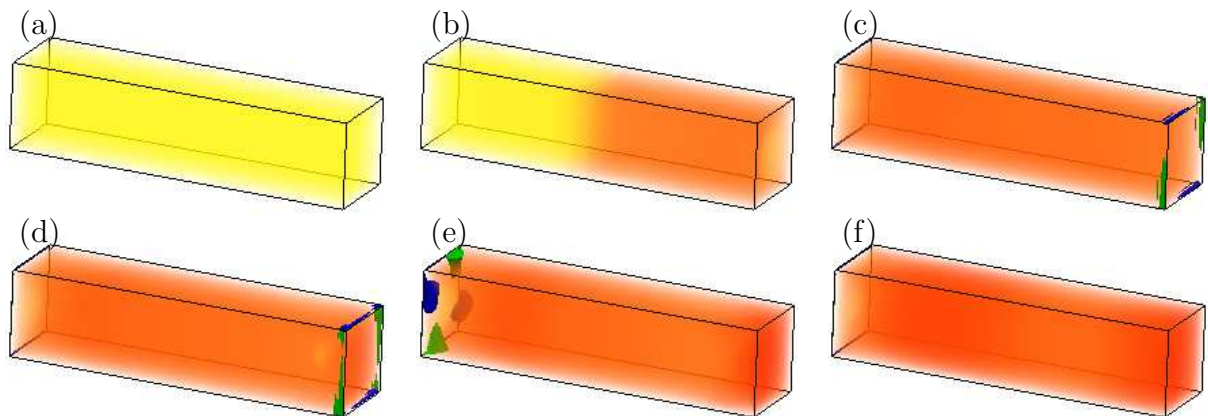

Figure 9: (Color online) PE: microstructure morphology evolution in the nanowire under type III loading path at time instants t (ns) (a) 0, (b) 0.033, (c) 0.1167, (d) 0.133, (e) 0.183, (f) 0.416 (red, blue, green, and yellow colors represent M_1, M_2, M_3, and A variants, respectively). Transparent colors are used to investigate evolution of different variants.

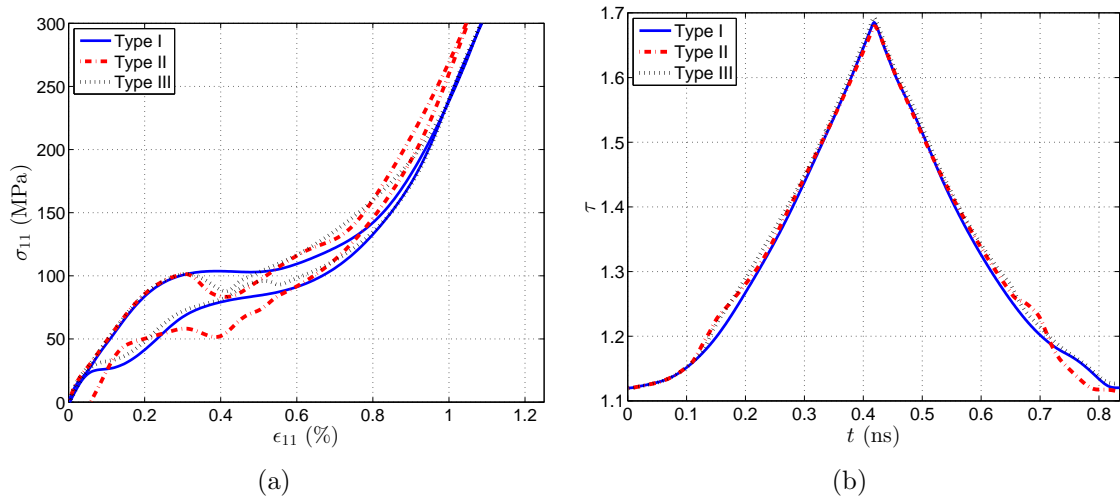Figure 10: (Color online) PE: average σ_{11}–ϵ_{11} (a) and time evolution of τ (b) for the type I, II and III multiaxial loading paths.

References

[1] K. Bhattacharya, *Microstructure of Martensite: why it forms and how it gives rise to the shape-memory effect.* Oxford University Press, 2003.

[2] D. Lagoudas, *Shape Memory Alloys: Modeling and Engineering Applications.* London: Springer, 2008.

[3] K. Otsuka and C. Wayman, *Shape memory materials.* Cambridge University Press, 1998.

[4] D. Fang, W. Lu, and K. Hwang, "Pseudoelastic behavior of CuAINi single crystal under biaxial loading," *Metals and Materials International*, vol. 4, no. 4, pp. 702–706, 1998.

[5] Y. Shan, J. Dodson, S. Abraham, J. Speich, R. Rao, and K. Leang, "A biaxial shape memory alloy actuated cell/tissue stretching system," in *Proc. ASME Intl. Mech. Eng. Congress and Expo*, pp. 161–169, 2007.

[6] S. Miyazaki, Y. Fu, and W. Huang, *Thin film shape memory alloys: fundamentals and device applications.* Cambridge University Press, 2009.

[7] T. Niendorf, J. Lackmann, B. Gorny, and H. Maier, "In-situ characterization of martensite variant formation in Nickel-Titanium shape memory alloy under biaxial loading," *Scripta Materialia*, 2011.

[8] R. Smith, *Smart material systems: model development*, vol. 32. Society for Industrial Mathematics, 2005.

[9] D. C. Lagoudas, P. B. Entchev, P. Popov, E. Patoor, L. C. Brinson, and X. Gao, "Shape memory alloys, part ii: Modeling of polycrystals," *Mechanics of Materials*, vol. 38, no. 5-6, pp. 430 – 462, 2006. Shape Memory Alloys.

[10] M. Tokuda, S. Petr, M. Takakura, and M. Ye, "Experimental study on performances in Cu-based shape memory alloy under multi-axial loading conditions," *Materials Science Research International*, vol. 1, no. 4, pp. 260–265, 1995.

[11] P. Sittner, Y. Hara, and M. Tokuda, "Experimental study on the thermoelastic martensitic transformation in shape memory alloy polycrystal induced by combined external forces," *Metallurgical and Materials Transactions A*, vol. 26, no. 11, pp. 2923–2935, 1995.

[12] T. Lim and D. McDowell, "Mechanical behavior of an Ni-Ti shape memory alloy under axial-torsional proportional and nonproportional loading," *Journal of Engineering Materials and Technology*, vol. 121, p. 9, 1999.

[13] C. Bouvet, S. Calloch, and C. Lexcellent, "Mechanical behavior of a Cu-Al-Be shape memory alloy under multiaxial proportional and nonproportional loadings," *Journal of Engineering Materials and Technology*, vol. 124, p. 112, 2002.

[14] J. McNaney, V. Imbeni, Y. Jung, P. Papadopoulos, and R. Ritchie, "An experimental study of the superelastic effect in a shape-memory Nitinol alloy under biaxial loading," *Mechanics of Materials*, vol. 35, no. 10, pp. 969–986, 2003.

[15] K. Lavernhe-Taillard, S. Calloch, S. Arbab-Chirani, and C. Lexcellent, "Multiaxial shape memory effect and superelasticity," *Strain*, vol. 45, no. 1, pp. 77–84, 2009.

[16] C. Grabe and O. Bruhns, "Path dependence and multiaxial behavior of a polycrystalline niti alloy within the pseudoelastic and pseudoplastic temperature regimes," *International Journal of Plasticity*, vol. 25, no. 3, pp. 513–545, 2009.

[17] V. Birman, "Review of mechanics of shape memory alloy structures," *Applied Mechanics Reviews*, vol. 50, no. 11, pp. 629–645, 1997.

[18] A. Paiva and M. Savi, "An overview of constitutive models for shape memory alloys," *Mathematical Problems in Engineering*, vol. 2006, pp. 1–30, 2006.

[19] A. Khandelwal and V. Buravalla, "Models for Shape Memory Alloy Behavior: An overview of modelling approaches," *International Journal of Structural Changes in Solids - Mechanics and Applications*, vol. 1, no. 1, pp. 111–148, 2009.

[20] M. Tokuda, M. Ye, M. Takakura, and P. Sittner, "Thermomechanical behavior of shape memory alloy under complex loading conditions," *International Journal of Plasticity*, vol. 15, no. 2, pp. 223–239, 1999.

[21] C. Bouvet, S. Calloch, and C. Lexcellent, "A phenomenological model for pseudoelasticity of shape memory alloys under multiaxial proportional and nonproportional loadings," *European Journal of Mechanics-A/Solids*, vol. 23, no. 1, pp. 37–61, 2004.

[22] F. Thiebaud, M. Collet, E. Foltete, and C. Lexcellent, "Implementation of a multi-axial pseudoelastic model to predict the dynamic behavior of shape memory alloys," *Smart materials and structures*, vol. 16, p. 935, 2007.

[23] H. Pan, P. Thamburaja, and F. Chau, "Multi-axial behavior of shape-memory alloys undergoing martensitic reorientation and detwinning," *International Journal of Plasticity*, vol. 23, no. 4, pp. 711–732, 2007.

[24] J. Arghavani, F. Auricchio, R. Naghdabadi, A. Reali, and S. Sohrabpour, "A 3-D phenomenological constitutive model for shape memory alloys under multiaxial loadings," *International Journal of Plasticity*, vol. 26, no. 7, pp. 976–991, 2010.

[25] A. Saleeb, S. Padula II, and A. Kumar, "A multi-axial, multimechanism based constitutive model for the comprehensive representation of the evolutionary response of SMAs under general thermomechanical loading conditions," *International Journal of Plasticity*, vol. 27, no. 5, pp. 655–687, 2011.

[26] L. Chen, "Phase Field Models for Microstructure Evolution," *Annual Review of Materials Research*, vol. 32, pp. 113–140, 2002.

[27] A. Khachaturian, *Theory of structural transformations in solids*. New York, NY: John Wiley and Sons, 1983.

[28] R. Melnik, A. Roberts, and K. Thomas, "Modelling dynamics of shape-memory-alloys via computer algebra," *Mathematics and Control in Smart Structures, Proc. of SPIE*, vol. 3667, pp. 290–301, 1999.

[29] A. Artemev, Y. Jin, and A. Khachaturyan, "Three-dimensional phase field model of proper martensitic transformation," *Acta Materialia*, vol. 49, no. 7, pp. 1165 – 1177, 2001.

[30] V. Levitas and D. Preston, "Three-dimensional landau theory for multivariant stress-induced martensitic phase transformations. i. austenite $\leftrightarrow$ martensite," *Physical Review B*, vol. 66, no. 13, p. 134206, 2002.

[31] R. Ahluwalia, T. Lookman, and A. Saxena, "Dynamic Strain Loading of Cubic to Tetragonal Martensites," *Acta Mater*, vol. 54, pp. 2109–2120, 2006.

[32] L. Wang and R. Melnik, "Finite volume analysis of nonlinear thermo-mechanical dynamics of shape memory alloys," *Heat Mass Transfer*, vol. 43, no. 6, pp. 535–546, 2007.

[33] M. Bouville and R. Ahluwalia, "Microstructure and Mechanical Properties of Constrained Shape Memory Alloy Nanograins and Nanowires," *Acta Mater.*, vol. 56, no. 14, pp. 3558–3567, 2008.

[34] F. Daghia, M. Fabrizio, and D. Grandi, "A non isothermal Ginzburg-Landau model for phase transitions in shape memory alloys," *Meccanica*, vol. 45, pp. 797–807, 2010.

[35] R. Dhote, M. Fabrizio, R. Melnik, and J. Zu, "Hysteresis Phenomena in Shape Memory Alloys by Non-Isothermal Ginzburg-Landau Models," *Commun Nonlinear Sci Numer Simul*, vol. 18, pp. 2549–2561, 2013.

[36] A. Idesman, J. Cho, and V. Levitas, "Finite Element Modeling of Dynamics of Martensitic Phase Transitions," *Appl. Phys. Lett.*, vol. 93, no. 4, p. 043102, 2008.

[37] R. Dhote, R. Melnik, and J. Zu, "Dynamic thermo-mechanical coupling and size effects in finite shape memory alloy nanostructures," *Computational Materials Science*, vol. 63, pp. 105–117, 2012.

[38] R. Dhote, R. Melnik, and J. Zu, "Dynamics of shape memory alloy nanowires under multi-axial loading conditions," *Meccanica*, vol. 49, pp. 1561–1575, 2014.

[39] R. Dhote, H. Gomez, R. Melnik, and J. Zu, "3D Coupled Thermo-Mechanical Phase-Field Modeling of Shape Memory Alloy Dynamics via Isogeometric Analysis," 2014, submitted (available as arXiv:`1403.5612`).

[40] R. Dhote, H. Gomez, R. Melnik, and J. Zu, "Effect of Aspect Ratio and Boundary Conditions in Modeling Shape Memory Alloy Nanostructures with 3D Coupled Dynamic Phase-Field Models," 2014, submitted (available as arXiv:`1403.5608`).

[41] G. Barsch and J. Krumhansl, "Twin Boundaries in Ferroelastic Media without Interface Dislocations," *Phys. Rev. Lett.*, vol. 53, no. 11, pp. 1069–1072, 1984.

[42] G. Bales and R. Gooding, "Interfacial dynamics at a first-order phase transition involving strain: dynamical twin formation," *Physical review letters*, vol. 67, no. 24, p. 3412, 1991.

[43] J. Cottrell, T. Hughes, and Y. Bazilevs, *Isogeometric Analysis: Toward Integration of CAD and FEA*. John Wiley & Sons., 2009.

[44] S. Kartha, J. A. Krumhansl, J. P. Sethna, and L. K. Wickham, "Disorder-driven pretransitional tweed pattern in martensitic transformations," *Phys. Rev. B Condens. Matter.*, vol. 52, pp. 803–822, 07 1995.

[45] E. Pieczyska, S. Gadaj, W. Nowacki, and H. Tobushi, "Thermomechanical investigations of martensitic and reverse transformations in tini shape memory alloy," *Bulletin of the Polish Academy of Sciences Technical Sciences*, vol. 52, no. 3, 2004.

[46] E. Pieczyska, S. Gadaj, W. Nowacki, and H. Tobushi, "Phase-transformation fronts evolution for stress-and strain-controlled tension tests in tini shape memory alloy," *Experimental Mechanics*, vol. 46, no. 4, pp. 531–542, 2006.

[47] J. Rejzner, C. Lexcellent, and B. Raniecki, "Pseudoelastic behaviour of shape memory alloy beams under pure bending: experiments and modelling," *Int J Mech Sci*, vol. 44, no. 4, pp. 665–686, 2002.